

# Zero-field magnetometry based on the combination of atomic orientation and alignment

Gwenael Le Gal<sup>1,2\*</sup> and Agustin Palacios-Laloy<sup>1</sup>

1. *Univ. Grenoble Alpes, CEA, Leti, F-38000 Grenoble, France and*

2. *Univ. Grenoble Alpes, CNRS, Grenoble INP, G2Elab, F-38000 Grenoble, France*

Optically pumped magnetometers usually rely on optical pumping using circularly- or linearly-polarized light. We study here zero-field magnetometers pumped with elliptically-polarized light, preparing both atomic orientation and alignment with complementary geometries. We start by extending the “three-step approach” for elliptically-polarized pumping. This allows us studying the Hanle effect in elliptical polarization by comparing the analytical absorption signals with experiments made on helium-4 metastable state. We then study parametric resonance magnetometers based on elliptical polarization by using the dressed-atom formalism with one and two radio-frequency fields. The results show a good agreement with the experimental measurements and open interesting perspectives for magnetometry where symmetry breaking by pumping light is mitigated.

## I. INTRODUCTION

During the last years, optically pumped magnetometers (OPMs) operating in very low magnetic fields have reached excellent levels of sensitivity surpassing those of SQUIDS [1–3] without requiring cryogeny. Such sensors already proved their ability to measure ultra-low magnetic fields in several domains such as space exploration [4] or magnetic imaging of biological currents in cardiography [5, 6], fetal cardiography [7] and encephalography [8, 9].

Most of the vector zero-field OPMs configurations use circularly-polarized light [10–12] for pumping the atomic ensemble towards an oriented state, i.e. with average angular momentum  $\langle J_k \rangle \neq 0$  where  $\vec{k}$  is the propagation direction of the light. For atomic states with total angular momentum  $J \geq 1$ , such as the  $2^3S_1$  helium-4 ( $^4\text{He}$ ) metastable state, one can use linearly-polarized light to prepare atomic alignment (i.e. states with  $\langle 3J_e^2 - \vec{J}^2 \rangle \neq 0$  where  $\vec{e}$  is the direction of the pump-light electric field  $\vec{E}_0$  [13]). In both cases, the symmetry breaking by the optical pumping prevents from measuring the magnetic field component longitudinal to the pumping direction ( $\vec{k}$  for orientation,  $\vec{e}$  for alignment) with a good sensitivity.

Since elliptically-polarized light has both circular and linear polarization components, it can be used for pumping the atomic ensemble towards states that are both oriented and aligned. In a recent communication [14], this kind of polarization combined to parametric resonances [15, 16] resulting from two radio-frequency (RF) magnetic fields allowed measuring the three components of the magnetic field with isotropic sensitivity.

Our purpose here is to provide an in depth study of the physics of zero-field magnetometers based on elliptically-polarized light.

To do so, we focus first (in Sec. II) on the Hanle effect of an ensemble pumped using elliptically-polarized light, in analogy to the studies of Castagna and Weis [17] for orientation and Breschi and Weis [18] for alignment. For elliptical pumping light Hanle resonances exist for all components of the magnetic field. The amplitudes and widths of these resonances depend on the pumping light ellipticity, which allows an interesting analysis of the relaxation rates of the different atomic multipoles.

From this study we deduce (in Sec. III) a theoretical description of a single-RF field parametric resonance magnetometer (PRM) based on elliptically-polarized light by using the dressed atom formalism [15, 16, 19].

The dressed atom formalism also allows studying an atomic ensemble subject to several RF fields [15, 16], a configuration which allows the measurement of several components of the magnetic field. We present these calculations in Sec. IV. These predictions are in good agreement with the experimental measurements. We will also discuss the choices of parameters—ellipticity, RF fields directions, frequencies and amplitudes—which are optimal for obtaining a three-axis vector magnetometer with isotropic sensitivity.

## II. HANLE EFFECT OF A SPIN-1 ATOMIC STATE PUMPED WITH ELLIPTICALLY-POLARIZED LIGHT

### A. Theory

Hanle effect is a well-known phenomenon, which consists in resonant variations of the optical properties of a polarized atomic ensemble as a function of the magnetic field [20]. Such resonances only appear when the magnetic field  $B_0$  is very small ( $\gamma B_0 \ll \Gamma$ , where  $\gamma$  is the gyromagnetic ratio and  $\Gamma$  is the relaxation rate of the Zeeman coherences,  $-2\pi \times 28 \text{ s}^{-1} \cdot \text{nT}^{-1}$  and  $\sim 5 \text{ ms}^{-1}$  respectively for the  $2^3S_1$  state of helium-4), and when the atomic polarization is transverse to it [21, 22]. Our goal here is to calculate the absorption signals resulting

\* gwenael.legal@yahoo.fr

from the Hanle effect for any polarization of the pumping light, and with respect to all the components of the magnetic field.

We consider the setup of Fig. 1.a, in which an ensemble of  $^4\text{He}$  atoms in the metastable state are subject to optical pumping using elliptically-polarized light tuned on the  $D_0$  transition ( $2^3S_1 \rightarrow 2^3P_0$ ). In order to describe the atomic polarization, we decompose the metastable state density matrix  $\rho$  of the ensemble on the irreducible tensor operators (ITO) basis:

$$\rho = \sum_{k=0}^{2J} \sum_{q=-k}^k m_q^{(k)} \hat{T}_q^{(k)\dagger} \quad (1)$$

with  $m_q^{(k)} = \langle \hat{T}_q^{(k)} \rangle$  the atomic multipole moments,  $\hat{T}_q^{(k)}$  the irreducible tensors operators and  $J = 1$  for the  $2^3S_1$  state. The rank  $k = 0$  describes the total state population, rank  $k = 1$  the atomic orientation, and rank  $k = 2$  the atomic alignment. In the following, we set the quantization axis along the light propagation direction  $\vec{z}$ .

First, we want to derive a simple expression of the absorption signals. For this purpose, we use the so-called three step approach, broadly used in atomic magnetometry, which consists in modeling the dynamics of the atomic polarization as it was happening in three steps: (i) atomic state preparation by optical pumping, (ii) state evolution under magnetic field and relaxation, and (iii) measurement of the system state. This simplification allows obtaining a good picture of the ensemble evolution as far as the pumping-light intensity is low enough [23–25], i.e.  $\Gamma_p \ll \Gamma_e$ , where  $\Gamma_e$  is the relaxation rate of the metastable state due to collisions with the cell walls and other species in the plasma, and  $\Gamma_p$  is the optical pumping rate as defined in the references [26–28].

We will also make a few more reasonable approximations. The  $^4\text{He}$  metastable state is populated by a high-frequency electrical discharge (Sec. II B). We assume that the discharge has reached a steady-state so that the metastable population is constant. We also assume that the population of the  $2^3P_0$  is negligible as compared to the one of  $2^3S_1$ , since the relaxation rate of the former is much larger than the one of the latter.

Within those approximations, the dynamics of the metastable state can be described by the following equation:

$$\left[ \frac{d}{dt} - \mathbb{H}(\vec{B}) + \Gamma \right] M = \Gamma_p M_p \quad (2)$$

for ranks  $k = 1$  and  $k = 2$  [16, 18, 29, 30]. In this equation,  $\Gamma = \Gamma_e + \Gamma_p$ ,  $M$  is the multipole moments

tensor, i.e. the orientation vector  $(m_{-1}^{(1)}, m_0^{(1)}, m_1^{(1)})^t$  for  $k = 1$ , and the five-components alignment column matrix  $(m_{-2}^{(2)}, m_{-1}^{(2)}, m_0^{(2)}, m_1^{(2)}, m_2^{(2)})^t$  for  $k = 2$ .  $\mathbb{H}(\vec{B})$  is the magnetic evolution matrix, which for  $k = 1$  is given in Appendix A and for  $k = 2$  is given in the references [16, 30].  $M_p$ —with components  $m_{q,p}^{(k)}$ —is the steady-state multipole moments tensor resulting from optical pumping alone, in the absence of magnetic field and relaxation. For rank  $k = 0$  we have constant population  $m_0^{(0)} = 1/\sqrt{2J+1} = 1/\sqrt{3}$  [31].

In the usual cases when pumping with light is purely circularly- or linearly-polarized the expressions of  $M_p$  are well known [16, 30, 32][31, Eq. 4.61 and 4.62]. For elliptical polarization, the expression of  $M_p$  needs to be carefully derived as a function of the light ellipticity.

With the setup shown in Fig. 1.a: the resulting elliptically-polarized light has its major axis along  $\vec{y}$  and ellipticity  $\varphi$  ( $\alpha = 0$  and  $\varepsilon = \varphi$  in the so-called  $\alpha - \varepsilon$  parametrization [33]). Following Omont [34, Eq. 3.1] this leads to the following non-zero components of  $M_p$ :<sup>1</sup>

$$\begin{aligned} m_{0,p}^{(1)} &= \frac{1}{2\sqrt{2}} \sin(2\varphi) \\ m_{0,p}^{(2)} &= -\frac{1}{2\sqrt{6}} \\ m_{\pm 2,p}^{(2)} &= \frac{1}{4} \cos(2\varphi). \end{aligned} \quad (3)$$

When the light is strictly speaking elliptically-polarized ( $\varphi \neq 0^\circ, 45^\circ$ ) both a longitudinal orientation and a transverse alignment are created in the atomic gas, the latter along the ellipse major axis. The complete steady-state solutions of Eq. 2 using Eq. 3 are given in Appendix B.

We can now calculate the photodetection signals. For the setup of Fig. 1.a and an optically thin ensemble, the absorption coefficient  $\kappa$  is [35]:

$$\begin{aligned} \kappa \propto 2 \left( \frac{m_0^{(0)}}{\sqrt{3}} + \frac{m_0^{(2)}}{\sqrt{6}} \right) - 2 \sin(2\varphi) \frac{m_0^{(1)}}{\sqrt{2}} \\ - 2 \cos(2\varphi) \left( \frac{m_{-2}^{(2)} + m_2^{(2)}}{2} \right). \end{aligned} \quad (4)$$

The state population  $m_0^{(0)}$  and the longitudinal alignment  $m_0^{(2)}$  always contribute to  $\kappa$ . Otherwise depending on the relative strength between circular and linear polarization the signal may be dominated by the longitudinal orientation  $m_0^{(1)}$  or the transverse alignment  $m_{\pm 2}^{(2)}$ .

For the Hanle effect (Eqs. B1, B2 and B3) the absorption coefficients are:

<sup>1</sup> Note that our definition of the steady-state multipole moments

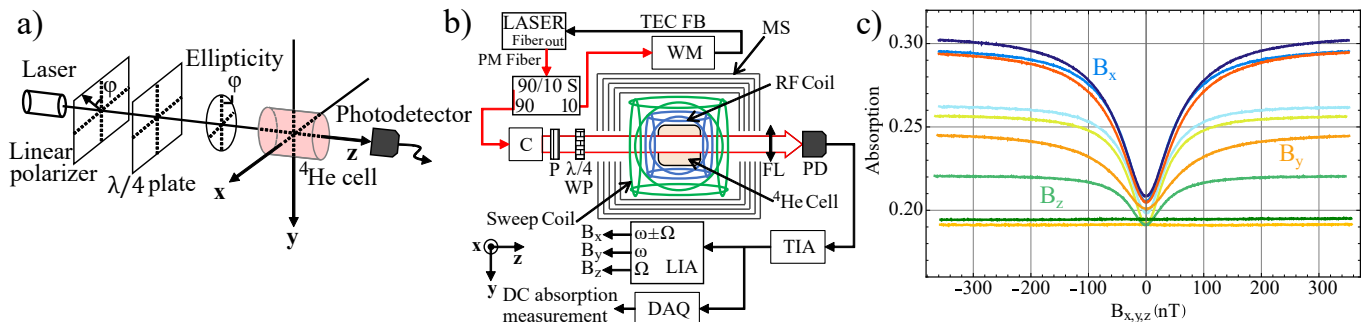


Figure 1. Theoretical and experimental study of Hanle effect resonances in  $^4\text{He}$  atoms pumped with elliptically-polarized light. (a) Geometrical configuration considered for the optical pumping of the  $^4\text{He}$  ensemble with elliptically-polarized light. The light goes through a linear polarizer, forming an angle  $\varphi$  with the  $\vec{y}$  axis, and a quarter waveplate with fast axis parallel to  $\vec{y}$  before entering the  $^4\text{He}$  cell. (b) Experimental setup. PM: Polarization maintaining; TEC FB: TEC Feedback; WM: Wavelength Meter; MS: Magnetic Shield; 90/10 S: 90/10 Splitter; C: Collimator; P: Linear Polarizer; WP: Waveplate; FL: Focusing Lens; PD: InGaAs Photodiode; TIA: Transimpedance Amplifier; LIA: Lock-In Amplifier; DAQ: DAQmx Board. The redlined paths show the optical paths and the black ones the electrical signal paths. (c) Hanle effect resonances observed experimentally when sweeping  $B_x$  (blue),  $B_y$  (orange) and  $B_z$  (green) at different ellipticities:  $\varphi = 0^\circ$  (lighter colors),  $\varphi = 25^\circ$  (middle shade colors) and  $\varphi = 45^\circ$  (darker colors). See the text for the description of the experiment.

$$\kappa_{Hanle}(\omega_z, \omega_{x,y} = 0) \propto \frac{2(\Gamma - \Gamma_p)(\Gamma^2 + 4\omega_z^2) + 6\Gamma_p\omega_z^2 \cos^2(2\varphi)}{3\Gamma(\Gamma^2 + 4\omega_z^2)} \quad (5)$$

$$\kappa_{Hanle}(\omega_x, \omega_{z,y} = 0) \propto \frac{2}{\Delta_x} \left\{ (\Gamma - \Gamma_p)(\Gamma^4 + 5\Gamma^2\omega_x^2 + 4\omega_x^4) + \Gamma_p \cos^2(\varphi) [3\Gamma^2\omega_x^2 + 3\omega_x^4(1 + 3\sin^2(\varphi))] \right\} \quad (6)$$

$$\kappa_{Hanle}(\omega_y, \omega_{z,x} = 0) \propto \frac{2}{\Delta_y} \left\{ (\Gamma - \Gamma_p)(\Gamma^4 + 5\Gamma^2\omega_y^2 + 4\omega_y^4) + \Gamma_p \sin^2(\varphi) [3\Gamma^2\omega_y^2 + 3\omega_y^4(1 + 3\cos^2(\varphi))] \right\} \quad (7)$$

where  $\Delta_i = 3\Gamma(\Gamma^4 + 5\Gamma^2\omega_i^2 + 4\omega_i^4)$ , with  $i \in \{x, y\}$ ,  $\omega_{x,y,z} = -\gamma B_{x,y,z}$  is the Larmor angular frequency associated with the  $x, y$  or  $z$  component of the magnetic field.

For every components of the magnetic field, there is an even-symmetric absorption signals. The only exceptions are  $\kappa_{Hanle}(\omega_z, \omega_{x,y} = 0)$  that is constant with  $\varphi = 45^\circ$ , and  $\kappa_{Hanle}(\omega_y, \omega_{z,x} = 0)$  which is constant when  $\varphi = 0^\circ$ .

First, we have compared these expressions to the experimental measurements of Hanle effect resonances (Sec. II B). This allowed some interesting observations on the relaxation rates. Secondly, we can use these Hanle effect dynamics as a basis to study the parametric resonance signals, since parametric resonance can be understood as the Hanle effect of the atom dressed by the RF fields [15].

---

is not the same as in Eq. 4 of Beato [28], both being related by  $M_{ss} = 2M_p$ . We made this choice in order to keep the usual physical meaning of the pumping steady-state (otherwise its corresponding density matrix has negative components). This choice requires rewriting the Eq. 4 of Beato as  $dM/dt = \mathbb{H}(\vec{B}) \cdot M - \mathbb{R} \cdot M + 2\Gamma_p M_p$ .

## B. Experimental study of the Hanle effect

The experimental setup is shown on Fig. 1.b. It consists of a 1-cm diameter and 1-cm length cylindrical cell filled with 9-Torr high purity helium-4. The  $2^3\text{S}_1$  metastable level is populated using a high-frequency (HF) capacitively-coupled electric discharge at 13.23 MHz, absorbing 27 mW of electrical power. We use an external cavity diode laser (Sacher Cheetah TEC 50), constantly tuned to the  $D_0$  line of  $^4\text{He}$ , at  $\lambda = 1083.206$  nm, by locking its temperature with a wavelength-meter (HighFinesse WS-7). The laser light is coupled in a polarization maintaining optical fiber and passes through a variable optical attenuator before being collimated using a converging lens to obtain a 7-mm diameter beam. A linear polarizer and a zero-order quarter wave plate (Thorlabs reference WPQ10M-1064), both mounted in independent rotation mounts, are placed before the helium cell to control the pumping light ellipticity. In the experiments reported here, the quarter wave plate fast-axis is set along  $\vec{y}$  and only the polarizer is rotated.

The helium cell is placed inside two sets of triaxial Helmholtz coils: the inner one is used to generate

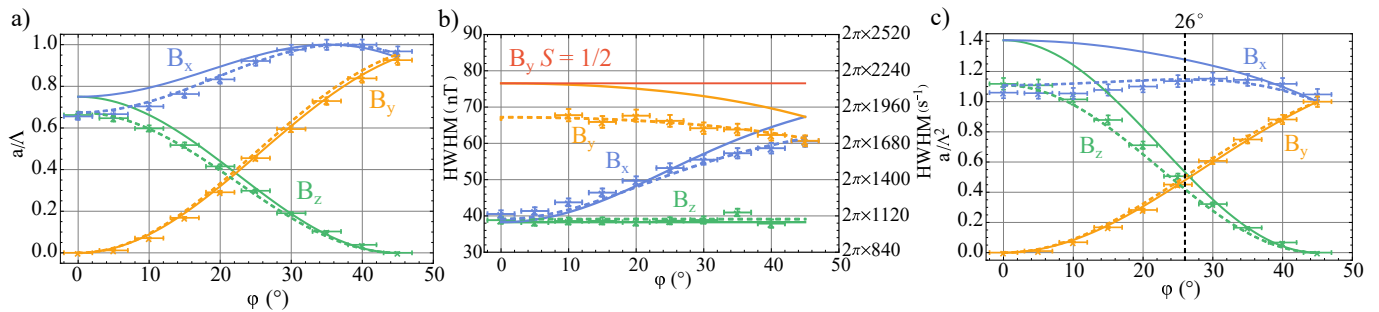


Figure 2. Study of the Hanle effect with elliptically-polarized pumping light. (a) Experimental (dots with error bars) and theoretical (solid and dashed lines) dependences of the amplitude of the Hanle resonances as a function of the pumping light ellipticity for  $B_x$  (blue),  $B_y$  (orange) and  $B_z$  (green). The experimental and theoretical data are normalized to the maximum amplitude. (b) Experimental and theoretical HWHMs of the Hanle resonances as a function of the light ellipticity. Red solid line: HWHM value of a spin-1/2 Hanle effect resonance at  $\varphi = 45^\circ$ . (c) Experimental and theoretical dependences of the PRM slope estimation  $a/\Lambda^2$  as a function of the light ellipticity. The experimental data and theoretical estimations are normalized to the value at  $\varphi = 45^\circ$  for  $B_y$ . The vertical black dashed line is set at the optimal ellipticity to measure the three component of the magnetic field simultaneously. For the three figures, the solid lines show the theoretical values of the model with isotropic  $\Gamma$ , with  $\Gamma_e = 53.3$  nT and  $\Gamma_p = 23.3$  nT. The dashed lines show the theoretical estimations with anisotropic  $\Gamma^{(k)}$ , calculated with  $\Gamma_p = 23.3$  nT,  $\Gamma_e^{(1)} = 43.9$  nT and  $\Gamma_e^{(2)} = 54.9$  nT.

the RF fields when exciting parametric resonances and the outer one is used to generate static magnetic field sweeps. The cell and coils are placed inside a five-layer  $\mu$ -metal cylindrical magnetic shield, whose longitudinal axis is along  $\vec{z}$ . A converging lens focuses the transmitted laser beam on an In-Ga-As photodiode connected to a homemade transimpedance amplifier (TIA) with gain 23.8 k $\Omega$ . Its output signal is acquired by a NI-DAQmx board for Hanle effect measurements, or demodulated with a Zürich MFLI lock-in amplifier for parametric resonances (see Sec. III and IV). For Hanle measurements, a first-order low-pass filter with 40 Hz cut-off frequency is inserted before the DAQmx board to attenuate the noise brought by the plasma discharge.

The three components of the magnetic field are sequentially swept with ramps of  $\pm 300$  nT at 1 Hz frequency. The optical power is set to  $\sim 300$   $\mu$ W at the cell input. The absorption is obtained as  $1 - V_{PD}/V_{PD,OFF}$ , where  $V_{PD}$  is the voltage at the TIA output during the magnetic field sweep, and  $V_{PD,OFF}$  is the voltage when the helium-4 discharge is off, which is measured before each acquisition.

Hanle effect signals for  $\varphi$  ranging from  $0^\circ$  (linear polarization along  $\vec{y}$ ) to  $45^\circ$  (circular polarization), and with respect to the three components of the magnetic field are shown in Fig. 1.c.

For every strictly speaking elliptical polarizations ( $\varphi \neq 0^\circ, 45^\circ$ ), Hanle resonances can be observed for all the three component of the magnetic field (e.g. middle shade colored lines in Fig. 1.c for  $\varphi = 25^\circ$ ).

We fit these curves with a Lorentzian function to obtain the amplitudes and Half-Width-Half-Maximum (HWHM), noted  $a/\Lambda$  and  $\Lambda$  respectively. The results are shown in Fig. 2.a and b, along with the theoretical predictions computed from Eqs. 5, 6 and 7 (solid lines). The theoretical HWHMs result from  $\Gamma = \Gamma_e + \Gamma_p$  and

Eqs. C2.  $\Gamma_e$  is estimated from the zero-field parametric resonance versus  $B_z$  with  $\varphi = 0^\circ$  at low optical power ( $P < 13$   $\mu$ W),  $\text{HWHM} = \Gamma/2$ . If  $\Gamma_p \ll \Gamma_e$ , the HWHM is close to  $\Gamma_e/2$ .  $\Gamma_p$  is estimated as  $(\text{HWHM} - \Gamma_e)$  at the optical power  $P \approx 300$   $\mu$ W used in the measurements.

There is a qualitative agreement between the theoretical expectations and the experiments. In Fig. 2.a, we see that the  $B_x$  resonance amplitude (orthogonal to the laser propagation direction  $\vec{z}$  and the quarter-wave plate fast axis  $\vec{y}$ ) increases with  $\varphi$ , and slightly decreases for  $\varphi > 40^\circ$ . The  $B_z$  and  $B_y$  resonances amplitudes show opposed behaviors as a function of  $\varphi$ :

- The  $B_z$  resonance amplitude decreases as  $\varphi$  increases. Hanle effect resonances being only present when the applied magnetic field is transverse to the atomic polarization direction [15, 30, 36], this behaviour seems natural for this resonance, linked to the alignment longitudinal to  $\vec{y}$ .
- The  $B_y$  resonance amplitude evolves in an opposite way, reaching a higher relative amplitude than the alignment Hanle resonance. We see in Fig. 2.b that the HWHM also varies with  $\varphi$ , witnessing a change of the kind of atomic polarization. It is well-known that optical pumping using circularly-polarized light of states with  $J > 1/2$  also creates alignment along the light propagation [17]. At low ellipticity, the signal is similar to the Hanle resonance of an oriented spin-1/2, which HWHM is  $\Gamma$ , twice the one of an aligned spin-1. When  $\varphi$  increases, the HWHM decreases due to the contribution of the alignment longitudinal<sup>2</sup> to  $\vec{z}$ . In

<sup>2</sup> The alignment contribution in Eq. 4, proportional to  $m_0^{(2)}$  and



other words, we observe the sum of the Hanle effect signals of an oriented spin-1/2 and an aligned spin-1.

- The  $B_x$  resonance amplitude does not cancel for any  $\varphi$ . Indeed, since this component is orthogonal to both orientation and alignment,  $B_x$  is always transverse to the atomic polarization. When  $\varphi < 40^\circ$ , both alignment along  $\vec{y}$  and orientation along  $\vec{z}$  (and some alignment along  $\vec{z}$ ) contribute to the Hanle resonance signal. The amplitude of the signal increases with  $\varphi$ , reaching its maximum at  $\varphi = \tan^{-1}(1/\sqrt{2}) \approx 35.2^\circ$ . For  $\varphi > 40^\circ$ , the alignment along  $\vec{y}$  becomes smaller and orientation along  $\vec{z}$  keeps increasing, yielding similar resonances as with  $B_y$ . The data of Fig. 2.b comforts this interpretation, showing that the  $B_x$  resonance HWHM goes from the one of an aligned state Hanle resonance to the one of a spin-1 pumped with circularly-polarized light.

Although the shape of the dependence is qualitatively good, there is not a good quantitative agreement between the theoretical predictions and the measurements. The Fig. 2.a show a good agreement for high ellipticities which worsens for  $\varphi < 30^\circ$ . Further analysis suggests that the discrepancies come from the isotropic nature of the relaxation rate  $\Gamma$  used as hypothesis. Through the method of Appendix D, this rate can be decomposed on  $\Gamma_e$  and  $\Gamma_p$  as shown in Fig. 3. As expected, the optical pumping rate  $\Gamma_p$  does not vary with  $\varphi$  because of the low enough optical power used. The relaxation rate  $\Gamma_e$  decreases with  $\varphi$ , witnessing a spin-dependent relaxation process of unknown nature.

We probed if including explicitly a spin-dependent relaxation in the model could improve the fit with experimental data. We calculated the resonance signals with anisotropic  $\Gamma$  by solving Eq. 2 with  $\Gamma^{(k)} = \Gamma_p + \Gamma_e^{(k)}$ . The expressions are cumbersome and not given here. The fit is made in several steps: first  $\Gamma_e^{(2)}$  is fitted from the HWHM variation with  $\varphi$  for the  $B_z$  resonances. Then  $\Gamma_e^{(1)}$  is fitted from the HWHM variation with  $\varphi$  for the  $B_x$  and  $B_y$  resonances. The result (Fig. 2, dashed lines) shows a much better agreement with the measurements.

The nature of this spin-dependent relaxation is unclear. A well-known spin-dependent relaxation process of the  $2^3S_1$  state in  $^4\text{He}$  plasma is Penning ionization, which is inhibited when all the atoms are prepared in the  $|+1\rangle$  or the  $|-1\rangle$  state. However, according to Ref. [37] the steady state electron density resulting from Penning ionization is proportional to  $n_0^2 + 2(n_1 n_0 + n_1 n_{-1} + n_0 n_{-1})$ ,

---

$m_{\pm 2}^{(2)}$ , has an amplitude varying as  $\sin^4(\varphi)/2$  and its HWHM is  $\Gamma/2$ . Similarly the orientation contribution, proportional to  $m_0^{(1)}$ , scales as  $\sin^2(2\varphi)/2$ , and its HWHM is  $\Gamma$ . As  $\varphi$  increases, the alignment contribution to the signal becomes more significant, thus reducing the amplitude and HWHM of the resonance.

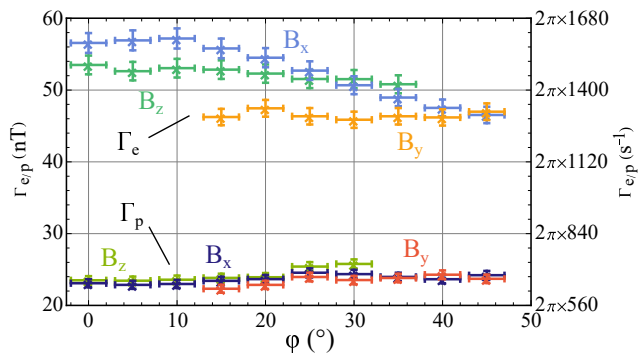


Figure 3. Dependence of the fitted natural relaxation rate  $\Gamma_e$  and the optical pumping rate  $\Gamma_p$  with the pumping light ellipticity  $\varphi$ . The values are obtained from the HWHM and amplitude measurements of Figs. 2.a and 2.b, as explained in Appendix D.

where  $n_i$  is the state population of the  $2^3S_1$  state Zeeman sub-level with  $m_z = i$ . This leads to a higher relaxation rate for metastable  $^4\text{He}$  atoms pumped with circularly-polarized light ( $n_{\pm 1} = 0$ ,  $n_{0,\mp 1} \neq 0$ ) than for linearly-polarized light ( $n_0 = 0$ ). We thus believe that other collisional processes in the helium plasma, maybe involving impurities, could be responsible for this unexpected behaviour. A similar behaviour related to impurities has been reported long ago with optically-pumped mercury [38].

### III. SINGLE-RF PARAMETRIC RESONANCE OF A SPIN-1 STATE PUMPED WITH ELLIPTICALLY-POLARIZED LIGHT

Let us briefly recall the zero-field parametric resonance phenomenon. For a spin-1/2 state, optically pumped with circularly-polarized light propagating along  $\vec{x}$  (Fig. 4.a), a transverse oscillating RF magnetic field  $B_{RF} \vec{z} \cos(\omega t)$  yields oscillating components in the photodetection signal at  $\omega$  and its harmonics. When sweeping  $B_z$  around the null field, the odd harmonics components show an odd-symmetric Lorentzian dependence with respect to  $B_z$ . Such a resonance can be observed with respect to the  $B_y$  component if the RF-field is applied along the  $\vec{y}$  axis, but not with the  $B_x$  component.

For a spin-1 aligned state, a similar resonance is observed when the applied RF field is transverse to the light polarization direction [16].

Parametric resonances based on circularly- and linearly-polarized pumping are broadly used to build compact vector OPMs, as they allow one to measure several components of the magnetic field using only one optical beam [12, 39, 40].

We study here parametric resonances when the pumping light is elliptically-polarized. A scheme of the different geometries we consider is shown in Fig. 4.b.

In Sec. II, we showed that using elliptically-polarized

pumping light on a spin-1 state leads to Hanle resonances for the three components of the magnetic field. Thus by applying an oscillating RF field, one can also observe parametric resonances for the three components of the

magnetic field. We can obtain the one-RF parametric resonance signals as a function of  $\varphi$  by using the dressed atom formalism [15, 16] and Eq. 2, yielding amplitudes of the component at frequency  $\omega$ :

$$\kappa_{1RF\parallel\vec{z},\omega}(\omega_z, \omega_{x,y} = 0) \propto \frac{2\Gamma_p J_{0,2} J_{1,2} \cos^2(2\varphi) \omega_z}{\Gamma^2 + 4\omega_z^2} \quad (8)$$

$$\kappa_{1RF\parallel\vec{x},\omega}(\omega_x, \omega_{y,z} = 0) \propto 2\Gamma_p \cos^2(\varphi) \left[ \frac{2J_{0,1} J_{1,1} \sin^2(\varphi)}{\Gamma^2 + \omega_x^2} + \frac{J_{0,2} J_{1,2} \cos^2(\varphi)}{\Gamma^2 + 4\omega_x^2} \right] \omega_x \quad (9)$$

$$\kappa_{1RF\parallel\vec{y},\omega}(\omega_y, \omega_{x,z} = 0) \propto 2\Gamma_p \sin^2(\varphi) \left[ \frac{2J_{0,1} J_{1,1} \cos^2(\varphi)}{\Gamma^2 + \omega_y^2} + \frac{J_{0,2} J_{1,2} \sin^2(\varphi)}{\Gamma^2 + 4\omega_y^2} \right] \omega_y \quad (10)$$

where the  $J_{n,q} = J_n(q\gamma B_{RF}/\omega)$  are the first kind  $n$ th-order Bessel functions.

The Fig. 5.a shows the experimentally measured slopes acquired at an optical power of approximately 240  $\mu$ W at the cell input. The RF field with  $\omega/2\pi = 40$  kHz is applied along the direction of the magnetic field sweep. The photodetection signal is demodulated at  $\omega/2\pi$  using a Zürich MFLI lock-in amplifier. The slopes are determined by a linear fit around zero field. The Fig. 5.b shows the experimentally measured  $\gamma B_{RF}/\omega$  ratio maximizing the signal slope as a function of  $\varphi$ , along with the theoretical predictions.

We obtain a qualitative agreement with the measurements. The slope variations with  $\varphi$  is close to the one expected from the  $a/\Lambda^2$  of Hanle resonances (Fig. 2.c, see Sec. IV A for details). The variations of the HWHM and the optimal  $B_{RF}$  witness the kind of atomic polarization which evolve in the magnetic field. For instance for the  $B_z$  resonance,  $\gamma B_{RF}/\omega = 0.54$  and it does not vary with  $\varphi$ , showing that parametric resonance is associated only to the alignment along  $\vec{y}$ . For the  $B_y$  resonance the ratio varies with  $\varphi$ , ranging from  $\gamma B_{RF}/\omega \approx 1.1$ —the optimum for a spin-1/2 oriented state—at low  $\varphi$  to 0.74 when the light is circularly polarized. This behavior is interesting: at low light ellipticity, the parametric resonance is mainly due to the orientation along  $\vec{z}$ . When  $\varphi$  increases, so does the alignment along  $\vec{z}$  and the optimum becomes closer to the one of a spin-1 state pumped with circularly polarized light. Finally for the  $B_x$  resonance, the  $\gamma B_{RF}/\omega$  ratio varies from 0.54 to 0.74, showing that at low  $\varphi$  the parametric resonance is dominated by the alignment along  $\vec{y}$ , and at higher  $\varphi$  by the orientation and alignment along  $\vec{z}$ .

The Fig. 5.c showing the resonances HWHM as a function of  $\varphi$  comforts those interpretations. The HWHM is constant with  $\varphi$  for the  $B_z$  resonance. For  $B_y$  the HWHM evolves from the one corresponding to an oriented spin-1/2 towards the one of a spin-1 pumped with

circularly-polarized light. Finally, for  $B_x$  the HWHM varies from the one of alignment resonance to the one of a spin-1 pumped with circularly-polarized light. As for the Hanle effect signals, the use of an isotropic relaxation rate on the model importantly contributes to the discrepancies between the theoretical predictions and the measurements.

#### IV. DOUBLE-RF PARAMETRIC RESONANCE MAGNETOMETER USING ELLIPTICALLY-POLARIZED PUMPING LIGHT

In this section, we study the dynamics of the spin-1 ensemble pumped with elliptically-polarized light when two RF fields are applied.

We first derive general expressions of the signals as a function of  $\varphi$  (Sec. IV B). Then we perform an experimental study focusing only on the optimal ellipticity value, found in [14]. As explained below this value can be inferred from Hanle resonances measurements.

##### A. Link between the Hanle resonances and the parametric resonances

Hanle absorption signals (Eqs. 5, 6 and 7) do not display linear dependence with any component of the magnetic field. However, when an oscillating RF field is applied (Sec. III), it leads to modulations in the absorbed light, some of which display such a linear dependence with the component of the field parallel to the RF field [15, 36].

By comparing the absorption coefficient of Hanle and parametric resonances, for a spin-1/2 state pumped with circularly-polarized light propagating along  $\vec{z}$ , one finds [15]:

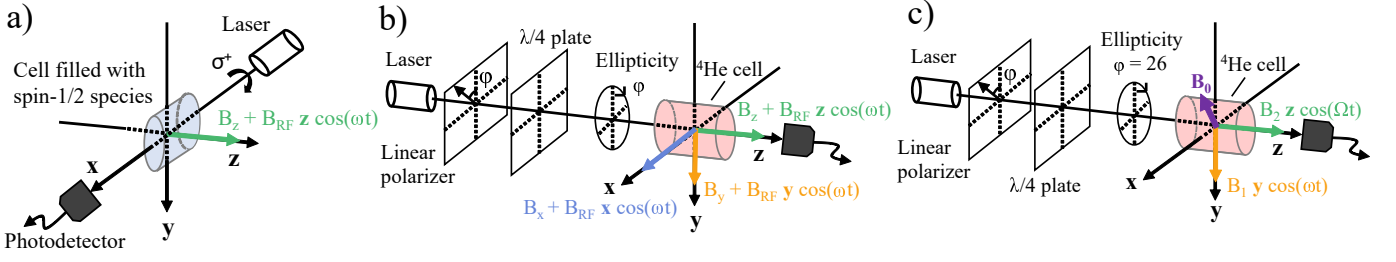


Figure 4. Schemes of the different PRMs geometries considered. (a) Scheme for a single-RF PRM using an oriented spin-1/2 atomic species. (b) Geometry considered in Sec. III for the study of single-RF parametric resonance in  $^4\text{He}$  as a function of  $\varphi$ . Only one component of the magnetic field and its parallel RF field are non-zero at once. (c) Geometry of the  $^4\text{He}$  elliptically-polarized light based PRM.  $\vec{B}_0$  is the static magnetic field to be measured.

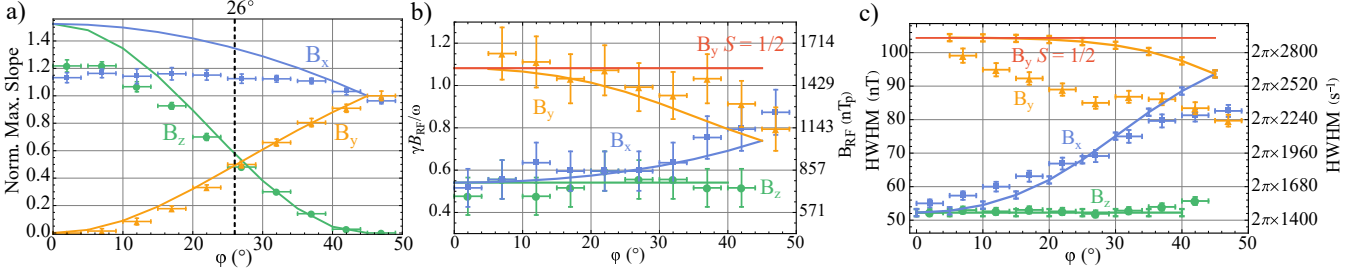


Figure 5. Study of the single-RF parametric resonance with elliptically-polarized pumping light. (a) Measured single-RF PRM signals slopes for the three axes along with the theoretical estimations as a function of  $\varphi$ .  $B_{RF}$  is chosen to maximize the slope. The experimental and theoretical values are normalized to their respective value for  $B_y$  at  $\varphi = 45^\circ$ . (b)  $B_{RF}$  maximizing the single-RF PRM signals slopes as a function of  $\varphi$ . (c) HWHM of the single-RF resonance at the  $B_{RF}$  value maximizing the slopes. The theoretical values are calculated by the very same method as for the Hanle resonances HWHMs (see Appendix C). The error bars of the theoretical estimations are due to the uncertainty on the optimal value of  $B_{RF}$ . The red line shows the theoretical value for an oriented spin-1/2 along  $\vec{z}$ .

$$\begin{aligned} \kappa_{1RF}^{\sigma^+}(\omega_x, \omega_y, z=0) &= 2J_{0,1}J_{1,1} \frac{a\omega_x}{\Gamma^2 + \omega_x^2} \\ &= 2J_{0,1}J_{1,1} \frac{\omega_x}{\Gamma} \kappa_{Hanle}^{\sigma^+}(\omega_x, \omega_y, z=0) \quad (11) \end{aligned}$$

where  $a$  is a coefficient related to the light properties only.

The slope  $\partial\kappa_{1RF}^{\sigma^+}/\partial B_x$  is proportional to the ratio  $a/\Gamma^2$  from Hanle resonances, which is however lowered by the  $J_{0,1}J_{1,1}$  factor. Thus, studying the dependence of  $a/\Gamma^2$  with  $\varphi$  yields an estimation of the best slope that can be reached for each  $\varphi$  for a single-RF PRM. This remains valid when a second RF field is applied, but with a prefactor comprising a more complicated combination of Bessel functions.

The Fig. 2.c shows the variations of  $a/\Lambda^2$  with  $\varphi$  (we here note the fitted HWHM as  $\Lambda$  to avoid confusion with  $\Gamma = \Gamma_e + \Gamma_p$ ). The variations closely follow the single-RF slopes shown on Fig. 5.a, which confirms that  $a/\Lambda^2$  is indeed an appropriate figure of merit of the PRM slope.

This allows us to obtain the optimal ellipticity for a two-RF PRM:  $\varphi = 26^\circ$ , where the slope to  $B_z$  equals the  $B_y$  one. At this ellipticity, the slope to  $B_z$  ( $B_y$  respectively) cannot be increased further without degrading the one to  $B_y$  ( $B_z$  respectively) while the slope to  $B_x$  is still higher than the two others.

## B. Two-RF PRM with $\varphi = 26^\circ$

We now study the dynamics when two oscillating RF fields are applied to  $^4\text{He}$  metastable atoms pumped using elliptically-polarized light with  $\varphi = 26^\circ$ .

In alignment-based PRMs, the two well-resolved components of the magnetic field are the ones parallel to the RF fields [16], which are applied orthogonally to the pumping direction (light polarization). This is the same for orientation-based PRMs, except that the pumping direction is along the light propagation [15].

When pumping with elliptically polarized light, each component of the magnetic field is orthogonal to either the orientation along  $\vec{z}$  ( $B_y$ ), the alignment longitudinal to  $\vec{y}$  ( $B_z$ ), or both of them ( $B_x$ ). Thus, the RF fields can be applied along these three directions, while keeping some sensitivity to all components of the magnetic field. In the previous section, we found that at  $\varphi = 26^\circ$  the slope to  $B_x$  is larger than the others. Since the dressing by a RF field reduces the sensitivity of the axes orthogonal to it [15, 16], the optimal directions for applying RF fields in our case seem to be the two orthogonal to  $B_x$ , so that the two less resolved components ( $B_y$  and  $B_z$ ) are less degraded than the best-resolved one ( $B_x$ ).

As shown in Fig. 4.c, we consider the two oscillating

RF fields  $\vec{B}_1 = B_1 \vec{y} \cos(\omega t)$  and  $\vec{B}_2 = B_2 \vec{z} \cos(\Omega t)$ , with  $\omega \gg \Omega \gg \Gamma, \gamma B_i$  [15]. The PRM signals can be

calculated from Eqs. 2, 3 in the doubly dressed-atom picture [15, 16], and Eq. 4. Keeping only first-order terms in magnetic field, we obtain for the component modulated at frequency  $\Omega$ :

$$\kappa_\Omega(\omega_z, \omega_x = \omega_y = 0) \propto \frac{\Gamma_p J_{0,1} [1 + 3 \cos(2\varphi) - 2J_{0,2} \sin^2(\varphi)]^2 \mathcal{J}_{0,2} \mathcal{J}_{1,2}}{8\Gamma^2} \omega_z + O(\omega_z^2) = s_z \omega_z + O(\omega_z^2) \quad (12)$$

For the component at frequency  $\omega$ :

$$\kappa_\omega(\omega_y, \omega_x = \omega_z = 0) \propto \frac{\Gamma_p \mathcal{J}_{0,1}^2 \sin^2(\varphi)}{4\Gamma^2} \{16J_{0,1} J_{1,1} \cos^2(\varphi) - J_{1,2} [(\mathcal{J}_{0,2} - 1)(1 + 3 \cos(2\varphi) - 2J_{0,2}(3 + \mathcal{J}_{0,2}) \sin^2(\varphi))]\} \omega_y + O(\omega_y^2) = s_y \omega_y + O(\omega_y^2) \quad (13)$$

And for their first inter-harmonic at  $\omega \pm \Omega$ :

$$\kappa_{\omega \pm \Omega}(\omega_x, \omega_y = \omega_z = 0) \propto \frac{\Gamma_p J_{0,1} \mathcal{J}_{0,1} \mathcal{J}_{1,1}}{4\Gamma^2} \{ [8J_{0,1} J_{1,1} \sin^2(2\varphi) + 2J_{1,2} \sin^2(\varphi) [(2J_{0,2}(3 - \mathcal{J}_{0,2}) \sin^2(\varphi) + (1 + \mathcal{J}_{0,2})(1 + 3 \cos(2\varphi))]] \} \omega_x + O(\omega_x^2) = s_x \omega_x + O(\omega_x^2) \quad (14)$$

where  $J_{n,q} = J_n(q\gamma B_1/\omega)$  and  $\mathcal{J}_{n,q} = J_n(qJ_{0,1}\gamma B_2/\Omega)$ .

The Fig. 6.a, b and c show the slopes measured for each component of the magnetic field as a function of the two RF fields amplitudes. The RF fields frequencies are  $\omega/2\pi = 40$  kHz and  $\Omega/2\pi = 9$  kHz, the optical power is set to approximately 250  $\mu$ W at cell input and we apply magnetic fields sweeps of  $\pm 90$  nT at 1 Hz frequency for the three components. The photodetection signal is then demodulated using a Zürich MFLI lock-in amplifier with reference signals at  $\omega$ ,  $\Omega$  and  $\omega \pm \Omega$  for  $B_y$ ,  $B_z$  and  $B_x$  respectively. These measurements can be compared to the theoretical predictions (Eqs. 12, 13 and 14) shown in Figs. 6.d, e and f.

There is a good agreement between the experiment and the theoretical expectations. A simple physical interpretation of this dynamics is not straightforward. The dressed-atom formalism shows that the dynamics is close to the one of Hanle effect, but in a generalized rotating frame [15]. We attempt here to give an interpretation of the observed behavior in this framework.

The slope  $s_y$ , is maximum where  $B_2 \approx 0$ . The dominant contribution is due to the orientation along  $\vec{z}$ .  $s_y$  depends on the RF field along  $\vec{z}$  with a  $\mathcal{J}_{0,1}^2$  prefactor, which has two origins: the dressing of  $B_y$  by  $\vec{B}_2$ , and the  $\overline{m}_{\pm 1}^{(k)}$  evolution<sup>3</sup> in  $\vec{B}_2$ . Both contributions reduce the slope, when  $\mathcal{J}_{0,1}^2 \neq 1$ , i.e. when  $B_2 \neq 0$ .

The slope  $s_z$  reaches the highest values among the three axes. It is enhanced by  $\vec{B}_1$ . In Eq. 12,  $s_z$  depends on  $B_1$  with  $J_{0,1}$  and  $J_{0,2}$  factors. The first one lowers  $s_z$  when  $B_1 \neq 0$ . Since  $\varphi = 26^\circ$ , if  $J_{0,2} = 1$  (i.e.  $B_1 = 0$ ),  $s_z$  decreases due to the  $[1 + 3 \cos(2\varphi) - 2J_{0,2} \sin^2(\varphi)]^2$  factor in Eq. 12. The compromise between the  $J_{0,1}$  and  $J_{0,2}$  contributions leads to an optimal  $s_z$  when  $B_1 \neq 0$ , so that  $J_{0,2} < 1$ .

Finally, there is a linear dependence at the first inter-harmonic  $\omega \pm \Omega$  with  $B_x$ . The slope  $s_x$  comes from the doubly-dressed atomic multipole moments bearing the linear dependence with  $B_x$  ( $\overline{m}_{\pm 1}^{(1),(2)}$ ). They are modulated once at the frequency of each RF field when coming back to the laboratory frame. At  $\varphi = 26^\circ$ ,  $s_x$  strongly benefits from both orientation and alignment, as expected from the Hanle effect measurements (Sec. II). This is the main origin of the slope increase for this axis—without parallel RF field—compared to the usual alignment- or orientation-based PRMs, allowing to reach isotropy with reasonable slope degradation [14].

It is finally interesting to discuss for which parameters such PRM scheme allows to obtain isotropic sensitivities (i.e.  $s_x \approx s_y \approx s_z$ ), as discussed in the reference [14].

The Fig. 7.a shows  $s = \sqrt{s_x^2 + s_y^2 + s_z^2}$  obtained from the experimental data presented in Figs. 6.a, b and c, along with the theoretical prediction for  $s$  (Fig. 7.b), and the experimentally measured  $s$  when  $\Omega/2\pi = 15$  kHz instead of 9 kHz (Fig. 7.c). The dotted area on the three figures shows the RF amplitudes values for which the “isotropic condition” (Eq. E1), as presented in Appendix E, is fulfilled.

The agreement between the theoretical predictions and

<sup>3</sup> The  $\overline{m}_q^{(k)}$  refer to the dressed atomic multipole moments before applying the rotation to come back to the laboratory frame and express the signal, for details see [15, 16].



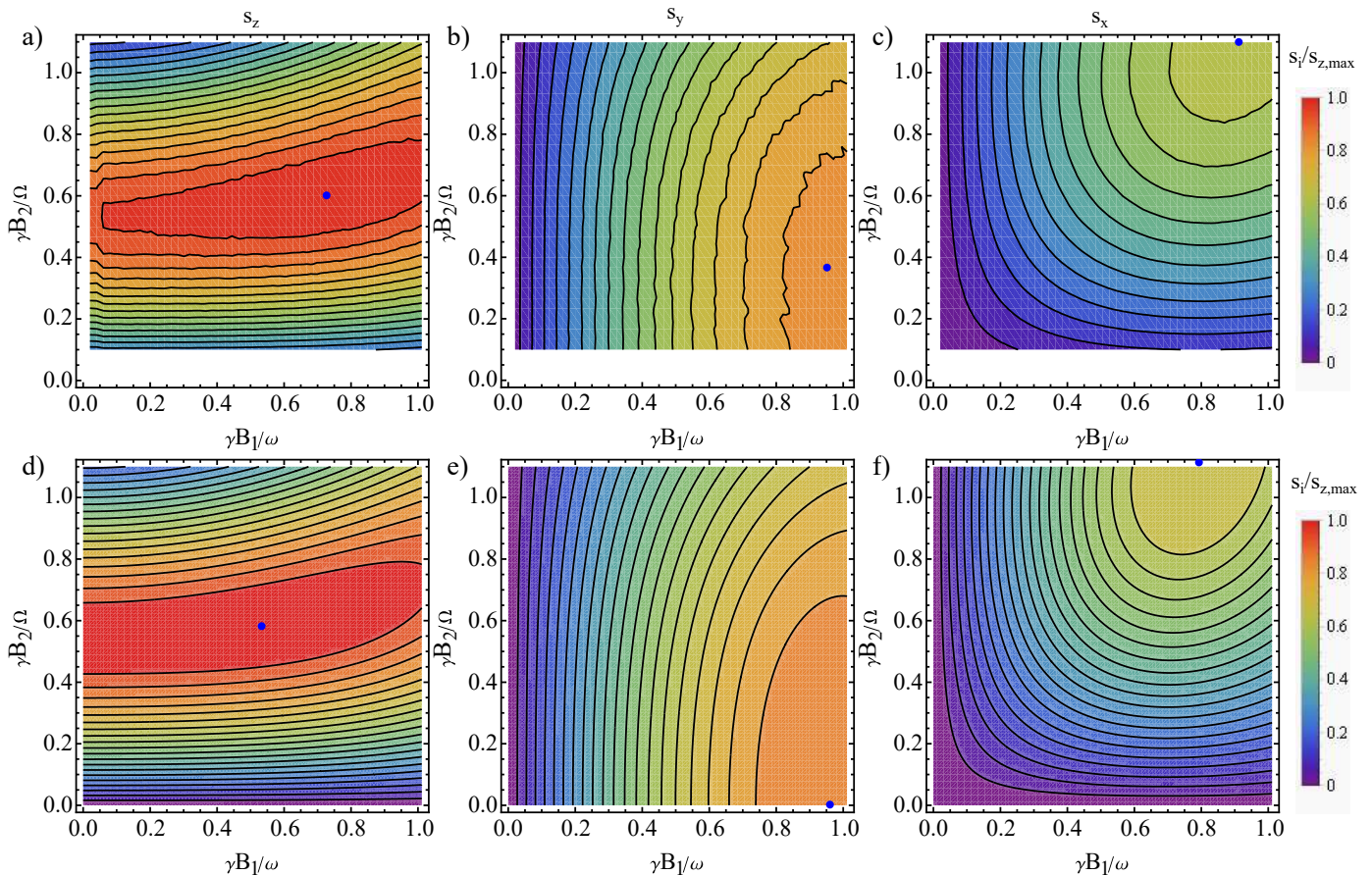


Figure 6. Slopes of the two-RF PRM based on elliptically-polarized light. (a), (b) and (c): Experimentally measured slopes  $s_z$ ,  $s_y$  and  $s_x$ , respectively, as a function of the RF fields amplitudes, ranging from  $B_1 = 58 \text{ nT}_p$  to  $1444 \text{ nT}_p$  ( $\Leftrightarrow \gamma B_1/\omega = 0.04$  to  $1.01$ ) for the fast RF field ( $\omega/2\pi = 40 \text{ kHz}$ ), and from  $B_2 = 32.1 \text{ nT}_p$  to  $353 \text{ nT}_p$  ( $\Leftrightarrow \gamma B_2/\Omega = 0.1$  to  $1.1$ ) for the slow RF field ( $\Omega/2\pi = 9 \text{ kHz}$ ). The blue dots show the position of the maximum slope for each axis. The three figures are normalized to the maximum slope reached among the three axes,  $s_{z,max}$ , corresponding to the blue dot of Fig. 6.a. (d), (e) and (f): Theoretical estimations of  $s_z$ ,  $s_y$  and  $s_x$ , respectively. The blue dots show the position of the maximum slope for each axis. The three figures are normalized with the maximum slope computed among the three axes,  $s_{z,max}$  (blue dot on Fig. 6.d).

the measurement at  $\Omega/2\pi = 9 \text{ kHz}$  is good, both for the values of  $s$  and for the region of isotropy. However, the  $(B_1, B_2)$  regions for which the isotropic sensitivity condition is fulfilled do not overlap the ones where  $s$  is maximum. Surprisingly we found that increasing  $\Omega/2\pi$  to  $15 \text{ kHz}$  allows obtaining this overlap [14]. As shown by the green dot in Fig. 7.c, the RF amplitudes leading to optimal isotropic slopes are  $B_1 = 1385 \text{ nT}_p$  ( $\gamma B_1/\omega = 0.97$ ) and  $B_2 = 407 \text{ nT}_p$  ( $\gamma B_2/\Omega = 0.76$ ). At these RF amplitudes, this is obtained mostly thanks to an increase of  $s_x$  when  $\Omega/2\pi = 15 \text{ kHz}$  compared to  $9 \text{ kHz}$ , and leads to a higher absolute value of  $s$  in addition of bringing the isotropic area where  $s$  is maximum.

The Figs. 7.b and c show that the theoretical predictions are not anymore in good agreement with the measurements, mostly concerning the isotropic area. Moreover, the theoretical model does not explain the observed increase of  $s_x$  with a larger  $\Omega$ .

A further experimental study shows that this increase seems to come from an influence of resonances adjacent

to the zero-field one, which lie at  $\gamma B_x = (\omega - \Omega)/2$ , being therefore closer to  $B_x = 0$  when  $\Omega/2\pi = 15 \text{ kHz}$  as shown in Fig 8.a. When  $\Omega$  is so that  $2\Omega < \omega - \Omega$ , there is a new resonance for  $\gamma B_x < (\omega - \Omega)/2$ , which is absent when  $2\Omega > \omega - \Omega$  at least at low RF amplitudes (Fig 8.b). This resonance seems to separate the zero-field resonance from the one at  $\gamma B_x = (\omega - \Omega)/2$ . At the RF fields amplitudes of the green dot in Fig 7.c, all these resonances are broadened and shifted towards higher values of  $B_x$ . For  $\Omega/2\pi = 15 \text{ kHz}$ , they are less shifted and other resonances of unknown nature are visible between  $B_x = 0$  and  $\gamma B_x = (\omega - \Omega)/2$ . These broadened and shifted adjacent resonances seem to be beneficial for  $s_x$  when  $\Omega/2\pi = 15 \text{ kHz}$ , whereas they lie at larger values of  $B_x$  when  $\Omega/2\pi = 9 \text{ kHz}$ , and thus have less influence on the zero-field resonance (Fig 8.c). If these resonances are broadened when the coupling increases, as magnetic resonances are, the resonances observed when  $\Omega/2\pi = 9 \text{ kHz}$  would be less broadened than when  $\Omega/2\pi = 15 \text{ kHz}$  because  $B_2$  is lower in the former case in order to have

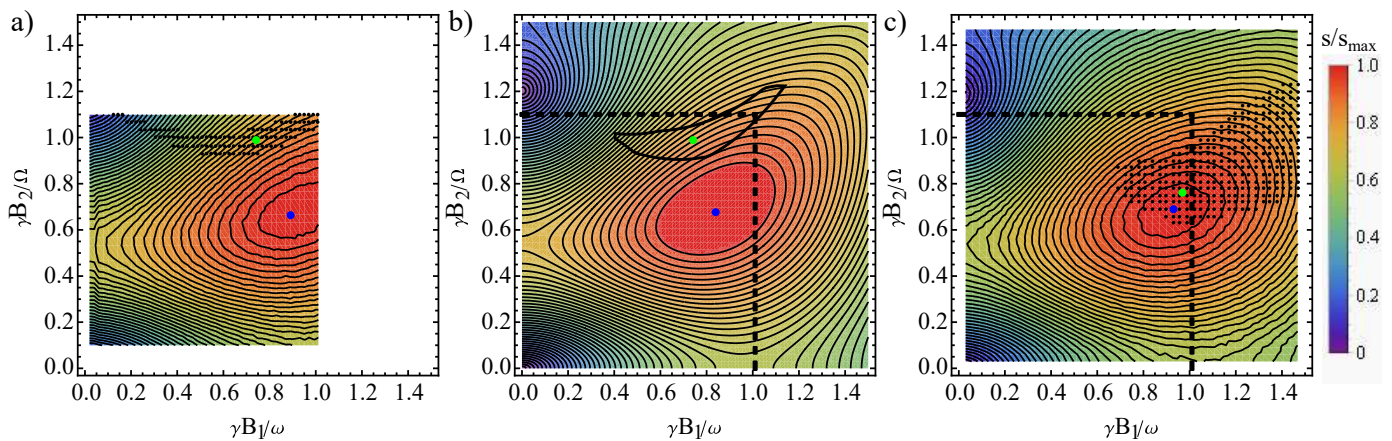


Figure 7. (a) Experimental dependence of  $s$  with the RF fields amplitudes, for  $\omega/2\pi = 40$  kHz and  $\Omega/2\pi = 9$  kHz. The values are normalized to the maximum value  $s_{max}$  (blue dot which coordinates are  $\gamma B_1/\omega = 0.89$ ,  $\gamma B_2/\Omega = 0.67$ ). The green dot is where  $s_x \approx s_y \approx s_z$ , and has coordinates  $\gamma B_1/\omega = 0.74$ ,  $\gamma B_2/\Omega = 0.99$ . The black dotted area is where the isotropic condition Eq. E1 is fulfilled. (b) Theoretical estimations of  $s$  with the RF fields amplitudes. The values are normalized with the maximum value  $s_{max}$  (blue dot which coordinates are  $\gamma B_1/\omega = 0.84$ ,  $\gamma B_2/\Omega = 0.68$ ). The green dot is where  $s_x = s_y = s_z$ , and has coordinates  $\gamma B_1/\omega = 0.74$ ,  $\gamma B_2/\Omega = 0.99$ . The solid black contoured area is where the isotropic condition is fulfilled. The black dashed square delimits the area of Fig. 7.a. (c) Experimental dependence of  $s$  with the RF fields amplitudes, for  $\omega/2\pi = 40$  kHz and  $\Omega/2\pi = 15$  kHz. The values are normalized with the maximum value  $s_{max}$  (blue dot which coordinates are  $\gamma B_1/\omega = 0.93$ ,  $\gamma B_2/\Omega = 0.69$ ). The green dot shows the RF amplitudes for which  $s_x \approx s_y \approx s_z$  (i.e.  $I_x \approx I_y \approx I_z \approx 0.33$ , see Appendix E), which has coordinates  $\gamma B_1/\omega = 0.97$ ,  $\gamma B_2/\Omega = 0.76$ . The black dotted area is where the isotropic condition is fulfilled. The black dashed square delimits the area of Fig. 7.a.

$\gamma B_2/\Omega = 0.76$ .

A more thorough understanding of these influences require supplementary experimental characterizations as well as a refinement of the theory presented here, accounting for the resonances other than the zero-field one.

## V. CONCLUSION

In conclusion, we presented here how to compute in the three-step approach formalism the Hanle resonance signals for any closed  $J = 1 \rightarrow J' = 0$  optical transition excited with elliptically-polarized light. The obtained expressions are in qualitative good agreement with the presented measurements. We showed that the difference can be explained from a dependence of the relaxation rate in the dark with the pumping light ellipticity, probably coming from some collisional processes in the helium discharge. The introduction of an anisotropic relaxation rate for orientation and alignment leads to theoretical results much closer to the experiments.

PRMs signals can be deduced from Hanle effect signals using the dressed-atom formalism. We gave the single-RF PRM absorption signals as a function of the light ellipticity pumping a spin-1 atomic state. We also obtained the two-RFs PRM absorption signals dependence with the light ellipticity for a specific choice of the oscillating fields direction, which is the optimal configuration in order to achieve a PRM with isotropic sensitivity. These expressions show a good agreement with the experiments as long as the  $\Omega \ll \omega$  approximation is fairly

fulfilled, showing that this model allows understanding the dynamics of spin-1 atoms optically pumped with elliptically-polarized light under several non-resonant oscillating RF fields.

## ACKNOWLEDGMENTS

The authors acknowledge R. Romain for his help improving the manuscript, L.-L. Rouve, G. Pignol, F. Bertrand, T. Jager, J.-M. Léger, M. Le Prado and E. Labyt for interesting discussions, and W. Fourcault for his help building the experimental setup. G. LG. acknowledges CEA-LETI DSYS Ph.D. funding. This research work was supported by the French ANR via Carnot funding.

### Appendix A: Expression of the rank $k = 1$ magnetic evolution matrix in the ITO basis

The expression  $\mathbb{H}(\vec{B})$  matrix for the rank  $k = 1$  in the  $\{m_{-1}^{(1)}, m_0^{(1)}, m_1^{(1)}\}$  basis is:

$$\mathbb{H}(\vec{B}) = -i\gamma \begin{pmatrix} -B_z & \frac{B_-}{\sqrt{2}} & 0 \\ \frac{B_+}{\sqrt{2}} & 0 & \frac{B_-}{\sqrt{2}} \\ 0 & \frac{B_+}{\sqrt{2}} & B_z \end{pmatrix} \quad (\text{A1})$$



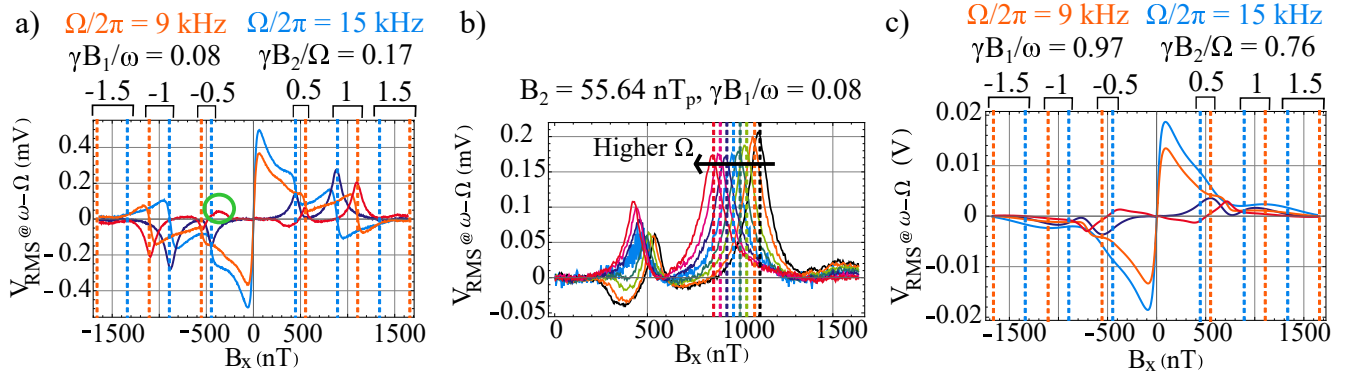


Figure 8. Resonances in the signal demodulated at  $\omega - \Omega$  for a large span  $B_x$  scanning with  $\omega/2\pi = 40$  kHz. (a) Resonances at low RF fields amplitudes. The unknown resonance appearing for  $\Omega/2\pi = 9$  kHz at  $B_x < (\omega - \Omega)/(2\gamma)$  is circled in green. (b) In-quadrature demodulated signal for different values of  $\Omega$ :  $\Omega/2\pi = 9$  kHz (black), 9.8 kHz (orange), 10.5 kHz (yellow), 11 kHz (light green), 12 kHz (deep green), 13 kHz (light blue), 14 kHz (deep blue), 15 kHz (pink), and 16 kHz (red). The vertical dashed lines show the value of  $(\omega - \Omega)/\gamma$ . (c) Resonances at the RF fields amplitudes of the green dot in Fig 7.c. For (a) and (c), the vertical dashed lines show the multiples  $n(\omega - \Omega)/\gamma$  for  $\Omega/2\pi = 9$  kHz in orange and  $\Omega/2\pi = 15$  kHz in blue, and the orange (light blue) and red (deep blue) lines show the in-phase and in-quadrature demodulated signals for  $\Omega/2\pi = 9$  kHz ( $\Omega/2\pi = 15$  kHz) respectively.

where  $B_{\pm} = B_x \pm iB_y$ .

### Appendix B: Expressions of the Hanle signals for arbitrary polarization of the pumping light

The steady-state solutions of Eq. 2 as a function the light ellipticity  $\varphi$  are:

$$\begin{aligned}
 m_0^{(1)}(\omega_z, \omega_{x,y} = 0) &= \frac{\Gamma_p \sqrt{2} \sin(2\varphi)}{\Gamma} \\
 m_0^{(2)}(\omega_z, \omega_{x,y} = 0) &= -\frac{\Gamma_p}{2\sqrt{6}\Gamma} \\
 m_{\pm 2}^{(2)}(\omega_z, \omega_{x,y} = 0) &= \frac{\Gamma_p \cos(2\varphi)}{4(\Gamma \mp 2i\omega_z)}
 \end{aligned} \tag{B1}$$

$$m_0^{(1)}(\omega_y, \omega_{x,z} = 0) = \frac{\Gamma \Gamma_p \sqrt{2} \sin(2\varphi)}{(\Gamma^2 + \omega_y^2)}$$

$$m_0^{(2)}(\omega_y, \omega_{x,z} = 0) = -\frac{\Gamma_p [\Gamma^2 + \omega_y^2 (1 + 3 \cos(2\varphi))]}{2\sqrt{6}\Gamma(\Gamma^2 + 4\omega_y^2)}$$

$$m_{\pm 2}^{(2)}(\omega_y, \omega_{x,z} = 0) = \frac{\Gamma_p [\Gamma^2 \cos(2\varphi) + \omega_y^2 (1 + 3 \cos(2\varphi))]}{4\Gamma(\Gamma^2 + 4\omega_y^2)} \tag{B2}$$

$$m_0^{(1)}(\omega_x, \omega_{z,y} = 0) = \frac{\Gamma \Gamma_p \sqrt{2} \sin(2\varphi)}{(\Gamma^2 + \omega_x^2)}$$

$$m_0^{(2)}(\omega_x, \omega_{z,y} = 0) = -\frac{\Gamma_p [\Gamma^2 + \omega_x^2 (-1 + 3 \cos(2\varphi))]}{2\sqrt{6}\Gamma(\Gamma^2 + 4\omega_x^2)}$$

$$m_{\pm 2}^{(2)}(\omega_x, \omega_{z,y} = 0) = \frac{\Gamma_p [\Gamma^2 \cos(2\varphi) + \omega_x^2 (-1 + 3 \cos(2\varphi))]}{4\Gamma(\Gamma^2 + 4\omega_x^2)}. \tag{B3}$$

### Appendix C: Expressions of the HWHM of Hanle resonances signals

The HWHMs expressions are evaluated as  $\omega_{x,y,z}$  solution of the equation

$$[\kappa_{Hanle}(\omega_{x,y,z} \rightarrow \infty) - [\kappa_{Hanle}(\omega_{x,y,z} \rightarrow \infty) - \kappa_{Hanle}(\omega_{x,y,z} = 0)] / 2] = \kappa_{Hanle}(\omega_{x,y,z}). \tag{C1}$$

This yields:

$$\begin{aligned} \text{HWHM}_x(\varphi) &= \frac{\Gamma \cos(\varphi)}{2} \sqrt{\frac{6[3 - 5 \cos(2\varphi)] + \sqrt{2[1331 - 1500 \cos(2\varphi) + 369 \cos(4\varphi)]}}{7 + 4 \cos(2\varphi) - 3 \cos(4\varphi)}} \\ \text{HWHM}_y(\varphi) &= \frac{\Gamma}{2} \sqrt{\frac{6[3 + 5 \cos(2\varphi)] + \sqrt{2[1331 + 1500 \cos(2\varphi) + 369 \cos(4\varphi)]}}{5 + 3 \cos(2\varphi)}} \\ \text{HWHM}_z(\varphi) &= \frac{\Gamma}{2} \end{aligned} \quad (\text{C2})$$

with  $\Gamma = \Gamma_e + \Gamma_p$  the total relaxation rate.

#### Appendix D: Determination of the relaxation rate and optical pumping rate from Hanle resonances signals

The natural relaxation rate  $\Gamma_e$  and the optical pumping rate  $\Gamma_p$  can be estimated from the experimental Hanle resonances by solving the following system:

$$\begin{cases} \frac{\kappa_{\text{Hanle}}(\omega_{x,y,z} = 0)}{\kappa_{\text{Hanle}}(\omega_{x,y,z} \rightarrow \infty)} = \frac{A(B_{x,y,z,0})}{A(B_{x,y,z} \gg \Gamma)} \\ \text{HWHM}_{x,y,z}(\varphi) = \Lambda_{x,y,z}(\varphi) \end{cases} \quad (\text{D1})$$

where  $A(B_{x,y,z,0}) = 1 - V_{\text{PD}}(B_{x,y,z,0})/V_{\text{PD,OFF}}$  is the minimum absorption measured at the value of the natural offset field component in the magnetic shield.  $A(B_{x,y,z} \gg \Gamma) = 1 - V_{\text{PD}}(B_{x,y,z} \gg \Gamma)/V_{\text{PD,OFF}}$  is the maximum asymptotic absorption value measured at the maximum magnetic field sweep value.  $\Lambda_{x,y,z}(\varphi)$  is the fitted HWHM for a given resonance. In the first equation, the ratio  $\kappa_{\text{Hanle}}(\omega_{x,y,z} = 0)/\kappa_{\text{Hanle}}(\omega_{x,y,z} \rightarrow \infty)$  takes the following values :

$$\begin{aligned} \frac{\kappa_{\text{Hanle}}(\omega_z, \omega_{x,y} = 0)}{\kappa_{\text{Hanle}}(\omega_z \rightarrow \infty, \omega_{x,y} = 0)} &= \frac{4\Gamma_e}{4\Gamma_e + 3\Gamma_p \cos^2(2\varphi)} \\ \frac{\kappa_{\text{Hanle}}(\omega_x, \omega_{z,y} = 0)}{\kappa_{\text{Hanle}}(\omega_x \rightarrow \infty, \omega_{z,y} = 0)} &= \frac{4\Gamma_e}{4\Gamma_e + 3\Gamma_p \cos^2(\varphi)(1 + 3 \sin^2(\varphi))} \\ \frac{\kappa_{\text{Hanle}}(\omega_y, \omega_{z,x} = 0)}{\kappa_{\text{Hanle}}(\omega_y \rightarrow \infty, \omega_{z,x} = 0)} &= \frac{4\Gamma_e}{4\Gamma_e + 3\Gamma_p \sin^2(\varphi)(1 + 3 \cos^2(\varphi))} \end{aligned} \quad (\text{D2})$$

#### Appendix E: Isotropic condition

$$\begin{cases} 0.37 > I_x > 0.3 \\ \quad \& \\ 0.37 > I_y > 0.3 \\ \quad \& \\ 0.37 > I_z > 0.3 \end{cases} \quad (\text{E1})$$

We define the condition of isotropic sensitivity on the slopes of the two-RF PRM as:

with  $I_i = |s_i| / (|s_x| + |s_y| + |s_z|)$  where  $i \in \{x, y, z\}$ . It is chosen so that the slope to each axis lies in  $\pm 10\%$  of  $1/3$  of the total slope.

- 
- [1] I. K. Kominis, T. W. Kornack, J. C. Allred, and M. V. Romalis, *Nature* **422**, 596 (2003).  
 [2] G. Vasilakis, H. Shen, K. Jensen, M. Balabas, D. Salart, B. Chen, and E. S. Polzik, *Nature Physics* **11**, 389 (2015).  
 [3] V. Shah, G. Vasilakis, and M. V. Romalis, *Physical Re-*

- view Letters* **104**, 013601 (2010).  
 [4] R. Slocum, *Revue de Physique Appliquée* **5**, 109 (1970).  
 [5] A. Weis, G. Bison, N. Castagna, S. Cook, A. Hofer, M. Kasprzak, P. Knowles, and J.-L. Schenker, *IFMBE Proceedings* **28**, 58 (2010).

- [6] S. Morales, M. C. Corsi, W. Fourcault, F. Bertrand, G. Cauffet, C. Gobbo, F. Alcouffe, F. Lenouvel, M. Le Prado, F. Berger, G. Vanzetto, and E. Labyt, *Physics in Medicine & Biology* **62**, 7267 (2017).
- [7] R. Wyllie, M. Kauer, R. T. Wakai, and T. G. Walker, *Optics Letters* **37**, 2247 (2012).
- [8] H. Xia, A. Ben-Amar Baranga, D. Hoffman, and M. V. Romalis, *Applied Physics Letters* **89**, 211104 (2006).
- [9] E. Labyt, M. C. Corsi, W. Fourcault, A. Palacios-Laloy, F. Bertrand, F. Lenouvel, G. Cauffet, M. Le Prado, F. Berger, and S. Morales, *IEEE Transactions on medical imaging* **38**, 90 (2019).
- [10] C. Cohen-Tannoudji, J. Dupont-Roc, S. Haroche, and F. Laloë, *Revue de Physique Appliquée* **5**, 102 (1970).
- [11] R. Jiménez-Martínez, S. Knappe, and J. Kitching, *Review of Scientific Instruments* **85**, 045124 (2014).
- [12] V. Shah, J. Osborne, J. Orton, and O. Alem, in *Steep Dispersion Engineering and Opto-Atomic Precision Metrology XI*, edited by S. M. Shahriar and J. Scheuer (SPIE, San Francisco, United States, 2018) p. 51.
- [13] Y. Shi and A. Weis, *The European Physical Journal D* **72**, 73 (2018).
- [14] G. Le Gal, L.-L. Rouve, and A. Palacios-Laloy, *Applied Physics Letters* **118**, 254001 (2021).
- [15] J. Dupont-Roc, *Journal de Physique* **32**, 135 (1971).
- [16] F. Beato, E. Belorizky, E. Labyt, M. Le Prado, and A. Palacios-Laloy, *Physical Review A* **98**, 053431 (2018).
- [17] N. Castagna and A. Weis, *Physical Review A* **84**, 053421 (2011).
- [18] E. Breschi and A. Weis, *Physical Review A* **86**, 053427 (2012).
- [19] G. Bevilacqua, V. Biancalana, A. Vigilante, T. Zanon-Willette, and E. Arimondo, *Physical Review Letters* **125**, 093203 (2020).
- [20] W. Hanle, *Zeitschrift fur Physik* **30**, 93 (1924).
- [21] C. Cohen-Tannoudji, J. DuPont-Roc, S. Haroche, and F. Laloë, *Physical Review Letters* **22**, 758 (1969).
- [22] D. Brazhnikov, S. Ignatovich, I. Mesenzova, A. Novokreshchenov, and A. Goncharov, *Optics Letters* **45**, 3309 (2020).
- [23] A. Weis, J. Wurster, and S. I. Kanorsky, *Journal of the Optical Society of America B* **10**, 716 (1993).
- [24] S. I. Kanorsky, A. Weis, J. Wurster, and T. W. Hänsch, *Physical Review A* **47**, 1220 (1993).
- [25] D. Budker, W. Gawlik, D. F. Kimball, S. M. Rochester, V. V. Yashchuk, and A. Weis, *Reviews of Modern Physics* **74**, 1153 (2002).
- [26] J. Barrat and C. Cohen-Tannoudji, *Journal de Physique et le Radium* **22**, 329 (1961).
- [27] P. J. Nacher and M. Leduc, *Journal de Physique* **46**, 2057 (1985).
- [28] F. Beato and A. Palacios-Laloy, *EPJ Quantum Technology* **7**, 9 (2020).
- [29] A. Weis, G. Bison, and A. S. Pazgalev, *Physical Review A* **74**, 033401 (2006).
- [30] G. Le Gal, G. Lieb, F. Beato, T. Jager, H. Gilles, and A. Palacios-Laloy, *Physical Review Applied* **12**, 064010 (2019).
- [31] K. Blum, *Density Matrix Theory and Applications*, Springer Series on Atomic, Optical, and Plasma Physics, Vol. 64 (Springer Berlin Heidelberg, Berlin, Heidelberg, 2012).
- [32] S. J. Seltzer, *Developments in Alkali-Metal Atomic Magnetometry*, Ph.D. thesis, Princeton University (2008).
- [33] M. Auzinsh, D. Budker, and S. Rochester, *Optically Polarized Atoms : Understanding Light-Atom Interactions* (New York : Oxford University Press, Oxford, 2010).
- [34] A. Omont, *Progress in quantum electronics* **5**, 69 (1977).
- [35] F. Laloë, M. Leduc, and P. Minguzzi, *Journal de Physique* **30**, 277 (1969).
- [36] C. Cohen-Tannoudji, J. Dupont-Roc, S. Haroche, and F. Laloë, *Revue de Physique Appliquée* **5**, 95 (1970).
- [37] M. V. McCusker, L. L. Hatfield, and G. K. Walters, *Physical Review Letters* **22**, 817 (1969).
- [38] J. Barrat, D. Casalta, J. Cojan, and J. Hamel, *Journal de Physique* **27**, 608 (1966).
- [39] A. P. Colombo, T. R. Carter, A. Borna, Y.-Y. Jau, C. N. Johnson, A. L. Dagel, and P. D. D. Schwindt, *Optics Express* **24**, 15403 (2016).
- [40] W. Fourcault, R. Romain, G. Le Gal, F. Bertrand, V. Josselin, M. Le Prado, E. Labyt, and A. Palacios-Laloy, *Optics Express* **29**, 14467 (2021).